Organic Electronics 13 (2012) 750–761

Contents lists available at SciVerse ScienceDirect

Organic Electronics

journal homepage: www.elsevier.com/locate/orgel

Coarse-grained kinetic modelling of bilayer heterojunction organic solar cells

Mosè Casalegno [a,*], Chiara Carbonera [b], Silvia Luzzati [c], Guido Raos [a]

[a] Dipartimento di Chimica, Materiali e Ingegneria Chimica "G. Natta", Politecnico di Milano, Via L. Mancinelli 7, 20131 Milano, Italy
[b] Research Center for Non-Conventional Energies, Istituto ENI Donegani, Eni S.p.A., Via G. Fauser 4, 28100 Novara, Italy
[c] Istituto per lo Studio delle Macromolecole, Consiglio Nazionale delle Ricerche, Via Edoardo Bassini 15, 20133 Milano, Italy

ARTICLE INFO

Article history:
Received 11 November 2011
Received in revised form 24 January 2012
Accepted 25 January 2012
Available online 10 February 2012

Keywords:
Organic solar cell
Kinetic Monte Carlo
Coarse-graining
Numerical simulations

ABSTRACT

The on-lattice kinetic Monte Carlo (KMC) method provides a powerful tool to simulate the *J–V* properties of organic solar cells. However, the computational cost associated with charge injection may limits its applicability. In the attempt to overcome this limitation, we describe in this paper a coarse-grained numerical approach to photocurrent generation in bilayer heterojunction solar cells. Starting from the KMC algorithm, a self-consistent numerical procedure is proposed to find the steady-state solutions of the kinetic equations describing particle dynamics in one dimension across the layer thickness. Our model incorporates the generation, transport and recombinations of charge carriers, excitons, and electron/hole pairs, whose introduction is required to correctly describe interfacial phenomena at the coarse-grained level. A continuum model of the electrostatic interactions among charge carriers is proposed and used to compute their hopping rates during the simulation. The model is used to investigate the *J–V* properties of Cathode/PCBM/P3HT/PEDOT:PSS/ITO bilayer devices, showing that Fermi level pinning at the Cathode/PCBM interface must be invoked to accurately model the experimental behavior. From the fitting to the experimental *J–V* data, we conclude the short-circuit current density to be mainly associated with a high exciton diffusion length. The analogies and differences between our model and existing KMC and drift–diffusion approaches are also discussed.

1. Introduction

Organic solar cells (OSCs) offer a promising and inexpensive alternative to silicon-based ones, in the race for renewable and environmentally friendly energy sources [1]. Although significant progress has been made since their discovery, OSCs are not yet ready for the energy market. The most efficient OSC to date have reached power conversion efficiencies of about 8–9% [2], close to the 10% efficiency considered necessary for beginning commercial exploitation. Different strategies are currently pursued with the aim of enhancing OSC competitiveness. The synthesis of new materials [3], new architectures [4] and the optimization of the processing conditions [5] provide possible routes to boost OSC performance. These strategies alone, however, cannot be exploited successfully without a good understanding of the physical processes underlying photocurrent generation in these devices. Computational studies can provide useful insights about these phenomena and, therefore, play an important role in the quest for higher efficiencies. The characterization of the relationship between device parameters and current–voltage (*J–V*) properties is of special interest, in view of the possibility to identify the factors limiting device efficiency.

The drift–diffusion (DD) [6] and the kinetic Monte Carlo (KMC) [7] methods are currently being applied by several groups to the numerical simulation of OSC's. Each

* Corresponding author.
E-mail addresses: mose.casalegno@chem.polimi.it (M. Casalegno), chiara.carbonera@eni.com (C. Carbonera), silvia.luzzati@ismac.cnr.it (S. Luzzati), guido.raos@polimi.it (G. Raos).

1566-1199/$ - see front matter © 2012 Elsevier B.V. All rights reserved.
doi:10.1016/j.orgel.2012.01.024

of these methods has its strengths and weaknesses. These rely on different levels of description and starting assumptions, which can be understood by considering their historical development. The DD method was originally developed for the simulation of inorganic (e.g. Si-based) field-effect transistors (FET's) and light-emitting diodes (LED's) [8]. It involves the search of the steady-state solutions to certain partial differential equations describing the densities and fluxes of charged particles and excitons. The use of a continuum mean-field description is almost natural for those devices, but its justification is certainly more problematic for an OSC, where typical charge carrier densities are orders of magnitude lower. Also, the description of charge extraction and injection at the electrodes involves some complex equations, typically derived from the Scott–Malliaras model of metal/semiconductor interfaces [9]. The KMC method is conceptually simpler and more general, but it is computationally more intensive. It does not adopt the continuum hypothesis, as it simulates the dynamics of the individual quasi-particles through random hopping events. It was first used to study some specific aspects of organic semiconducting materials, one example being Bässler's work on the effect of disorder on charge transport [10]. The application to whole OSC device models is much more recent and initially only addressed the behavior close to the short-circuit (SC) condition. The first full current–voltage (J–V) curves have appeared even more recently [11]. The main reason for this slow development is the difficulty of simulating the "dark current", which is related to charge injection close to the open-circuit (OC) condition.

The open-circuit voltage (V_{oc}) is a key parameter for the characterization of the performance of an OSC. By definition, no net current flows through the device under OC conditions. This occurs because the charges injected and extracted at the electrodes exactly balance each other. In KMC, charge injection is usually simulated by means of thermally activated hopping processes across the metal/organic interface. In practice, each electrode is discretized into a two-dimensional grid of charge-injecting sites, typically on the order of 10^4 for a 100×100 nm^2 surface. The injection rate for each site is assumed to be of the Miller–Abrahams type [12], so that the injection and extraction rates are related to each other by $e^{-\frac{\Delta}{k_B T}}$, where Δ is the barrier height. Owing to the large number of charge-injecting sites, decreasing Δ may increase the overall injection rate far beyond that of any other process. When this happens, the dynamical evolution of the system is dominated by the repeated occurrence of injection and extraction events [13]. Since the rate of these transitions can be orders of magnitude higher than that of all other events, the number of iterations necessary to adequately sample the configuration space soon becomes prohibitive. This exponential increase of CPU time is known to the KMC community as the "small-barrier" problem [14]. Accelerated approaches, such as AS-KMC [15], may eventually deal with this problem. Their application to OSC models has not yet been attempted, but in any case it does not necessarily guarantee reasonable computational efficiencies. In fact, an additional computational burden can be expected, due to the accumulation of charges close to the metal contacts under the effect of the image potential.

The issues outlined so far restrict the applicability of KMC to devices with moderately large injection barriers (0.4 eV) [11,16–18], and prevent the simulation of devices characterized by ohmic behavior. In the attempt to overcome these limitations, we propose in this paper a coarse-grained approach to photocurrent generation. The model adopts a one-dimensional representation of a bilayer device, which is derived from the three-dimensional one used in KMC simulations. Coarse-grained rates are developed from their microscopic analogs to describe the generation, transport and recombination of charge carriers and excitons. In analogy with DD methods [19–21], strongly bound electron–hole pairs are introduced to account for interfacial phenomena at the coarse-grained level. To overcome the small-barrier problem, the kinetic equations underlying the system dynamics are solved self-consistently. In this respect, our method resembles the so-called "master equation" approaches [22–26]. The electrostatic interactions among charge carriers are evaluated by a continuum model, developed from that used in three-dimensional KMC simulations. While in our previous KMC work where we were primarily concerned with an exact evaluation of the electrostatic interactions [27], our main aim here is to make contact with some real experimental data, and this has led us to a more approximate description in order to be computationally efficient. Henceforth, the present method will be denoted by 1DCG (one-dimensional coarse-grained).

The 1DCG model is naturally suited to the simulation of bilayer devices, for which there has recently been a resurgence of interest. In particular, Ayzner et al. [28] produced P3HT/PCBM bilayer devices with power conversion efficiencies up to 3.5%. In the same work, they also extensively characterized the bilayer morphologies, explicitly demonstrating by different microscopies the presence of a sharp and flat interface between P3HT and PCBM, which agrees with our model assumptions. On the other hand, the precise extent of this interfacial mixing is still a matter of debate. For example, Gevaerts et al. [29] have recently shown that annealed bilayers may outperform the bulk heterojunction devices with the same nominal composition and same total thickness, if partial intermixing at the interface occurs. Other potential advantages of bilayers over bulk heterojunctions are the greater ease of fabrication and morphological stability over time.

The following section introduces our computational model of the device and discusses our numerical methods. More technical aspects entering the calculation of electrostatic interactions are discussed in an Appendix. In the Results section, we apply the 1DCG model to the simulation of Cathode/PCBM/P3HT/PEDOT:PSS/ITO bilayers with high fill factors. These have been specially assembled using different Cathode materials, other things being equal. The model parameters are obtained by fitting the simulation results to the experimental J–V curves. We show that assuming Fermi level pinning at the Cathode/PCBM interface leads to the best fitting results. In agreement with

the interpretations of some experimental data [30], our results also suggest that the exciton diffusion length might be a key factor responsible for device efficiency. Finally, we discuss the analogies and differences between our model and existing KMC [11,16–18] and drift–diffusion [19–21] approaches.

2. Model

In this section we present a numerical model for photocurrent generation in bilayers, which is obtained by coarse-graining the conventional on-lattice KMC approach in both space and time. Spatially coarse-graining is generally used in KMC to extend the simulation length scale and reduce the CPU effort [31,32]. Here, conversely, it is mainly adopted to reduce the system dimensionality and simplify the kinetic equations associated with particle dynamics. To overcome the small barrier problem, these equations are solved in continuous – rather than discrete – time. As in master equation approaches [22–26], the electrostatic interactions among charge carriers are approximated by means of a continuum model. The development of this model, carried out in the Appendix, represents one innovative aspect of our approach.

2.1. Device representation

We consider a device with infinite periodic slab geometry. In an on-lattice KMC simulation, this would be represented by a simple cubic array of $M_x \times M_y \times M_z$ sites, to which periodic boundary conditions are applied along the x and y directions. Defining ℓ as the lattice constant, the position of a site (or a particle) in the device can be written as $\mathbf{r} = (x, y, z) = (m^x \ell, m^y \ell, m^z \ell)$, where (m^x, m^y, m^z) are integers with $m^x \in [1, M_x]$, $m^y \in [1, M_y]$, $m^z \in [0, M_z + 1]$. The layers of sites with $m^z = 0$ and $m^z = M_z + 1$ represent the cathode and the anode, respectively. In bilayer devices, the donor and acceptor materials form a planar interface. Its location is specified by an integer $L_z \in [2, M_z - 1]$. All the sites with $1 \leqslant m^z \leqslant L_z$ are acceptors (A), all those with $L_z + 1 \leqslant m^z \leqslant M_z$ are donors (D). Each site can be occupied by at most one quasi-particle (electron, hole or exciton).

Taking advantage of device symmetry, and neglecting the possibility of positional and energetic disorder [10], we spatially coarse-grain this three-dimensional grid into a one-dimensional one, by grouping all sites within the layer characterized by a certain value of m^z. In the new representation, the device appears as a collection of $M_z + 2$ layers, sequentially stacked on the top of each other along the z axis and separated from each other by ℓ. An example of such a representation is given in Fig. 1). The generic i-th layer comprises $M_{xy} = M_x \times M_y$ microscopic sites and is characterized by an overall occupancy number, $0 \leqslant N_i \leqslant M_{xy}$, that accounts for all kind of particles therein. These may be excitons (N_i^{ex}), electrons (N_i^{el}, only for A layers) and holes (N_i^{ho}, only for D layers), as in conventional KMC practice. In addition, if $i \in \{L_z, L_z + 1\}$, there may be some electrons and holes coulombically bound at the D/A interface (N^{gp}). These geminate pairs are introduced in the one-dimensional model to describe interface phenomena, as we shall see below. Cathode and anode act as charge reservoirs for electrons and holes, respectively. It is assumed that the carriers may freely flow through them, e.g. without affecting their occupancy, which is constant and equal to M_{xy}. The structure of the device and the contributions of the different kinds of particles to the occupancy of the layers are summarized in Table 1.

2.2. Coarse-graining the rates describing photocurrent generation

We now focus on the processes responsible for photocurrent generation. The conversion of light into electricity in OSC has been thoroughly described in a number of reviews [33] and in our previous article [27]. It is simulated in KMC by means of the events listed in Table 2. The rates at which these processes occur in three-dimensional KMC simulations usually refer to single sites, or to individual particles. All of these rates have analogs in the 1DGC model, and we shall derive them by an approach similar to that used by Dai et al. [32] in a different context. We shall see that the introduction of geminate pairs in the 1DCG model implies some additional events, which have no analogs in the KMC model.

To begin with, we consider exciton-related processes. In KMC simulations, the absorption of a photon immediately leads to the creation of one exciton in the photoactive layer. When optical interference effects are not considered, as it is often the case, the creation of excitons is uniform and may occur randomly at any unoccupied site with rate constant w^{exg}. The coarse-grained rate for this event can be obtained by summing the contributions of all the sites belonging to a layer. For the i-th layer, this leads to:

$$W_i^{exg} = w^{exg} M_{xy}(1 - \bar{\sigma}_i) \tag{1}$$

where $\bar{\sigma}_i \left(= \sum_{k \in \Omega_i} \sigma_k / M_{xy}\right)$ is the average occupancy of the i-th layer. Ω_i identifies all sites in the i-th layer, while σ_k is the occupancy (0 or 1) of the k-th site. Notice that we are

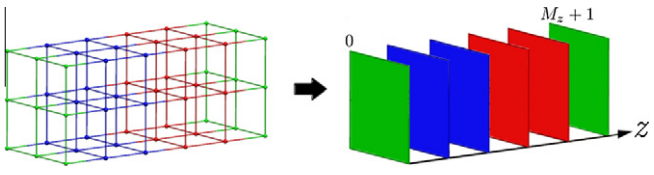

Fig. 1. Example of coarse-graining. A three-dimensional model device comprising few hopping sites (left) is coarse-grained into a one-dimensional one (right). Different colors are used to distinguish electrode (green), acceptor (blue), and donor (red) layers. For better clarity, the position of the electrodes along z is also shown. (For interpretation of the references to colour in this figure legend, the reader is referred to the web version of this article.)

Table 1
Device structure and layer occupancy numbers.

Material	i	N_i
Cathode	=0	$= N_i^{el} = M_{xy}$
Acceptor	$\in[1, L_z - 1]$	$= N_i^{el} + N_i^{ex}$
Interface (A)	$=L_z$	$= N_i^{el} + N_i^{ex} + N^{gp}$
Interface (D)	$=L_z + 1$	$= N_i^{ho} + N_i^{ex} + N^{gp}$
Donor	$\in[L_z + 2, M_z]$	$= N_i^{ho} + N_i^{ex}$
Anode	$=M_z + 1$	$= N_i^{ho} = M_{xy}$

Table 2
Overview of the KMC events in OSC modeling.

Event	Symbol
Exciton generation by light absorption	*exg*
Exciton diffusion by hopping	*exh*
Exciton decay	*exd*
Exciton separation at a D/A interface	*exs*
Electron/hole recombination	*ehr*
Electron (hole) transport via hopping	*elh* (*hoh*)
Electron (hole) collection at the cathode (anode)	*elc* (*hoc*)
Electron (hole) injection from the cathode (anode)	*ein* (*hin*)

using a lowercase letter (w) for the KMC rates, an uppercase letter (W) for the 1DGC ones. This may also be written:

$$W_i^{exg} = w^{exg}\ M_{xy}\ \theta_i \tag{2}$$

where θ_i is the fraction of unoccupied sites in the i-th layer:

$$\theta_i = \left(1 - \frac{N_i}{M_{xy}}\right). \tag{3}$$

Once generated, the excitons may diffuse isotropically via hopping between nearest-neighbor sites. We assume that they do not interact with the other particles (apart from the restriction preventing multiple occupancy of sites), nor with the electric field. Under these conditions, an expression for the attempt-to-hop frequency can be readily derived from the exciton diffusion coefficient D_{ex} [34]:

$$w^{exh} = 6\ D_{ex}/\ell^2. \tag{4}$$

On the original three-dimensional lattice, up to six destination sites are available to the hopping exciton. On average, only two out of six hops will contribute to its diffusion in the z direction. Therefore, on going to the one-dimensional model, the coarse-grained rate (from layer i to layer $j = i \pm 1$) becomes:

$$W_{i,j}^{exh} = \frac{1}{3} w^{exh} \theta_j [\delta_{i,j+1} + \delta_{i,j-1}]. \tag{5}$$

Eq. (5) refers to a single particle and should not be confused with the *overall* exciton hopping rate, $N_i^{ex} w^{exh} \theta_j$ one would use in coarse-grained KMC (CG-KMC) simulations [32]. The factor N_i^{ex} will be recovered in constructing the kinetic equation describing exciton dynamics. Note that, Eq. (5) prevent the diffusion of the excitons into electrodes, e.g. $W_{1,0}^{exh} = W_{M_z, M_{z+1}}^{exh} = 0$, according to the above assumptions (see Table 1).

In addition to hopping, an exciton may decay (in which case the absorbed photon is wasted) or, if it reaches either side of the D/A interface, it may dissociate into an electron–hole pair. The single-particle exciton decay rate within the layer is defined as $W^{exd} = w^{exd}$. The exciton diffusion length, L_{ex}, can be calculated from Eq. (4) as:

$$L_{ex} = \sqrt{6\ D_{ex}/w^{exd}}. \tag{6}$$

In KMC, the charge separation is accomplished by placing the electron on an A site and the hole on a neighboring D site. Owing to the low dielectric constant of organic materials (typically $\epsilon_r \simeq 2 - 3$), the newborn charges strongly interact with each other via the Coulomb potential. The resulting complex is characterized by spatially correlated carrier motions (the electron and hole "slide together" along the D/A interface [18,35]), which cannot be adequately described at the 1DGC level. To overcome this difficulty, we assume that exciton dissociation does not directly lead to free charges but rather to geminate electron–hole pairs. The rate at which this process occurs is, for a single exciton:

$$W^{exs} = w^{exs} \min\{\theta_{L_z}, \theta_{L_z+1}\}. \tag{7}$$

where the factor $\min\{\theta_{L_z}, \theta_{L_z+1}\}$ accounts for the occupancy of the interfacial layers. The rate constant w^{exs} is usually taken as the inverse of the exciton dissociation time, estimated at about 45 fs [33]. Geminate pairs may also form when an electron and a hole meet at opposite sides of the interface. The *overall* rate for this recombination process is assumed to be of the Langevin type [36]:

$$W^{ehr} = \frac{N_{L_z}^{el}\ N_{L_z+1}^{ho}}{M_{xy}\ell^3} \frac{e(\mu_0^{el} + \mu_0^{ho})}{\varepsilon_r \varepsilon_0} \tag{8}$$

where $\mu_0^{el(ho)}$ is the zero-field mobility of electrons (holes), e the elementary charge and ε_0 is the vacuum permittivity. The first term in Eq. (8) represents the effective density of carriers that may lead to geminate pair formation (e.g. those occupying nearest neighbours sites). Use of the Langevin formula in Eq. (8) is not completely correct, since it assumes that both carriers may diffuse in a homogeneous three-dimensional medium. Our choice is motivated by the need to supply our model with a simple equation describing electron–hole recombination at the interface. A number of studies [37] have shown the Langevin formula to overestimate the charge recombination efficiency. To account for this effect, additional calculations were performed after decreasing the recombination rate by a factor of ten. The model gave essentially the same results in terms of current density and V_{oc} position.

Like excitons, geminate pairs are treated as non-interacting particles. Once formed, a geminate pair can either decay or dissociate into free charge carriers with rates W^{gpd} and W^{gps}, respectively. The latter process produces free charge carriers at the interface layers. To simplify the implementation, we obtain its rate from those for charge hopping away from the interface, along the z axis:

$$W^{gps} = (w_0^{elh} + w_0^{hoh}) \exp\left(-\frac{\Delta E^{gps}}{k_B T}\right) \tag{9}$$

where ΔE^{gps} accounts for the effect of the external applied field (V_{ext}), the difference in electrode work functions ($\Delta\phi = \phi_{anode} - \phi_{cathode}$), and the change in the Coulomb potential energy:

$$\Delta E^{gps} = \frac{eV_{ext} - \Delta\phi}{M_z + 1} - \Delta C, \tag{10}$$

where:

$$\Delta C = \frac{e^2}{4\pi\varepsilon_r\varepsilon_0}\left(\frac{1}{2\ell} - \frac{1}{\ell}\right). \tag{11}$$

The diffusion of charge carriers is treated by the Miller–Abrahams hopping model [12], restricted to nearest-neighbor sites. In analogy with the case of exciton diffusion (Eq. (5)), we may write the 1DGC hopping rate as:

$$W_{i,j}^{elh(hoh)} = \frac{1}{3} w_0^{elh(hoh)} \overline{B}_{i,j}\theta_j[\delta_{ij+1} + \delta_{ij-1}]. \tag{12}$$

Here $w_0^{elh(hoh)}$ represents the maximum hopping rate of electrons (holes) [16]:

$$w_0^{elh(hoh)} = \frac{6k_BT\mu_0^{el(ho)}}{e\ell^2}. \tag{13}$$

The $\overline{B}_{i,j}$ factor accounts for the effect of the D and A energy levels and of the electric fields on the hopping rates. We use the following approximate expression:

$$\overline{B}_{i,j} = \begin{cases} 1, & \Delta\overline{E}_{i,j} \leqslant 0 \\ \exp\left(-\frac{\Delta\overline{E}_{i,j}}{k_BT}\right), & \Delta\overline{E}_{i,j} > 0 \end{cases} \tag{14}$$

where $\Delta\overline{E}_{i,j}$ is the average transition energy per particle. This is the sum of three contributions:

$$\Delta\overline{E}_{i,j} = \Delta\overline{E}^0_{i,j} + \Delta\overline{E}^F_{i,j} + \Delta\overline{E}^C_{i,j}. \tag{15}$$

$\Delta\overline{E}^0_{i,j}$ represents the average change in single-site energy associated with the HOMO (H) and LUMO (L) levels occupied by holes and electrons, respectively. Here we neglect the possibility of energy disorder (as in Bässler's Gaussian energy model [10]). All the acceptor sites have identical energy levels (E_A^H and E_A^L), similarly for the donor sites (E_D^H and E_D^L). Given this assumption, we may write:

$$\Delta\overline{E}^0_{i,j} = \begin{cases} E_j^L - E_i^L & \text{for electrons,} \\ E_i^H - E_j^H & \text{for holes.} \end{cases} \tag{16}$$

$\Delta\overline{E}^F_{i,j}$ accounts for the effect of an electric field directed along z, and can be written as:

$$\Delta\overline{E}^F_{i,j} = \pm\left(\frac{j-i}{M_z+1}\right)(eV_{ext} - \Delta\phi). \tag{17}$$

The + and − signs hold for holes and electrons, respectively. The last term, $\Delta\overline{E}^C_{i,j}$ accounts for the electrostatic interactions among charge carriers, including also their "images" within the metallic electrodes (see Appendix A). To confine electrons and holes in the respective phases (A for electrons, D for holes), we set:

$$W_{L_z,L_z+1}^{elh(hoh)} = W_{L_z+1,L_z}^{elh(hoh)} = 0. \tag{18}$$

Charge injection (*ein*, *hin*) and extraction (*elc*, *hoc*) are both treated as hopping processes. Their rates are evaluated according to Eq. (12). According to the assumptions made at the beginning of this Section, extraction rates are calculated setting $\theta_0 = \theta_{M_z+1} = 1$. The average energy levels of the electrodes in Eq. (16), E_0^L and $E_{M_z+1}^H$, are set to $-\phi_{cathode}$ and $-\phi_{anode}$, respectively.

2.3. The kinetic equations

We may now insert the coarse-grained rates derived above into the kinetic equations describing photocurrent generation in organic bilayer devices. It is worth noting that these rates could potentially be used to perform CG-KMC simulations. Use of this approach, however, would not solve the small-barrier problem detailed in the Introduction. To construct the kinetic equations, we consider the change in occupancy numbers due to the generation, transport, and recombination processes at each layer. The following set of equations is obtained:

$$\frac{dN_i^{ex}}{dt} = W_i^{exg} + N_{i-1}^{ex}W_{i-1,i}^{exh} + N_{i+1}^{ex}W_{i+1,i}^{exh} - N_i^{ex}\left(W_{i,i-1}^{exh} + W_{i,i+1}^{exh} + W^{exd}\right) \quad 1 \leqslant i \leqslant M_z \tag{19}$$

$$\frac{dN^{gp}}{dt} = (N_{L_z}^{ex} + N_{L_z+1}^{ex})W^{exs} + W^{ehr} - N^{gp}(W^{gpd} + W^{gps}) \quad i = L_z, L_z+1 \tag{20}$$

$$\frac{dN_i^{el}}{dt} = W_i^{elg} + N_{i-1}^{el}W_{i-1,i}^{elh} + N_{i+1}^{el}W_{i+1,i}^{elh} - N_i^{el}\left(W_{i,i-1}^{elh} + W_{i,i+1}^{elh}\right) \quad 1 \leqslant i \leqslant L_z \tag{21}$$

$$\frac{dN_i^{ho}}{dt} = W_i^{hog} + N_{i-1}^{ho}W_{i-1,i}^{ho} + N_{i+1}^{ho}W_{i+1,i}^{hoh} - N_i^{ho}\left(W_{i,i-1}^{hoh} + W_{i,i+1}^{hoh}\right) \quad L_z + 1 \leqslant i \leqslant M_z \tag{22}$$

where the time dependence of occupancy numbers has been dropped for convenience. To account for the generation of geminate pairs in Eqs. (19)–(22), exciton hopping rates across the D/A interface are modified as follows:

$$\begin{aligned} W_{i,i+1}^{exh} &= W^{exs}, W_{i+1,i}^{exh} = 0 \quad \text{for } i = L_z \\ W_{i,i-1}^{exh} &= W^{exs}, W_{i-1,i}^{exh} = 0 \quad \text{for } i = L_z + 1 \end{aligned} \tag{23}$$

The rates $W_i^{elg(hog)}$ in Eqs. (21) and (22) provide the net generation rate of charge carriers at the D/A interface:

$$W_i^{elg(hog)} = \begin{cases} 0 & \text{for } i \neq L_z\ (L_z+1) \\ N^{gp}W^{gps} - W^{ehr} & \text{for } i = L_z(L_z+1) \end{cases} \tag{24}$$

2.4. Numerical method

Eqs. (19)–(22) are solved iteratively to obtain the average occupancy numbers at steady state, and capture the *J*–*V* behavior of a bilayer device. The calculation begins by setting the occupancy numbers of all particles to zero, everywhere except at the electrodes. Based on these initial conditions, a first guess for the rate constants is obtained for a given value of the applied voltage, V_{ext}. At each iteration, exciton and charge carrier equations are solved first. Their occupancies are updated by a finite difference scheme with time steps of 0.01 ps and 5.0 ps, respectively.

Although generally not the most efficient, we found this method, along with the choice of different time steps, effective in avoiding the numerical instabilities related to the abrupt change in carrier densities in the first layers next to the electrodes. The number of geminate pairs is obtained from Eq. (20), setting $dN^{gp}/dt = 0$. The entire procedure is repeated until the steady state is reached. This occurs when the carrier fluxes through the electrodes balance the net carrier generation rates at the interface (see Eq. (24)). The following equations are used to calculate the electron and hole current densities at the electrodes:

$$\begin{aligned} J^{el} &= K_J \left(W^{elh}_{0,1} M_{xy} - W^{elh}_{1,0} N^{el}_1 \right) \\ J^{ho} &= K_J \left(W^{hoh}_{M_{z+1},M_z} M_{xy} - W^{hoh}_{M_z,M_{z+1}} N^{ho}_{M_z} \right) \end{aligned} \tag{25}$$

where $K_J = 1.602 \times 10^{10}/(M_{xy}\ell^2)$ [mA ps/cm^2], so that $J^{el(ho)}$ are expressed as [mA/cm^2]. Combining Eqs. (25) and (24), the following convergence criterion is obtained:

$$|J^{el} - K_J W^{elg}_{L_z}| < \Delta_J, \quad |J^{ho} - K_J W^{hog}_{L_z+1}| < \Delta_J \tag{26}$$

where the numerical threshold, Δ_J, is set to 10^{-3} mA/cm^2. At steady state, the total current is calculated as $J = J^{el} + J^{ho}$.

3. Experimental: device preparation and characterization

The 1DCG model is used in this work to investigate the *J–V* properties of three Cathode/PCBM/P3HT/PEDOT:PSS/ITO bilayers, using three different cathode materials. The devices were prepared starting from a transparent anode made by a pre-patterned ITO glass (Kintec, 17 Ω/square) with a PEDOT:PSS (Baytron P VP AL 4083) layer of 60 nm spin coated on top, dried on an hot-plate at 100 °C for 5 min in air and then inserted in a glove-box for further device assembling. The active layers were deposited by spin coating following a procedure developed by Ayzner et al. [28]. The P3HT (Plexcore OS2100) with high molecular weight (Mn: 62602 Mw: 119010) and 99% regioregularity was purchased from Plextronics. The polymer was dissolved in *o*-dichlorobenzene and kept at 50 °C overnight prior to spin coating into the PEDOT:PSS/ITO substrates. The film thickness, measured with a profilometer (Dektak) was 50 nm. After drying for at least 30 min, a PCBM overlayer (Solenne b.v.) of 30 nm was deposited from dichloromethane, a solvent for PCBM but not for P3HT. Prior to cathode evaporation, the deposited films were annealed on a hot plate at 150 °C for 30 min. The P3HT underlayer, prior to PCBM deposition and after washing out the fullerene layer, exhibited similar UV–Vis absorption spectrum and film thickness. These features, in agreement with previous results, are likely evidencing that the assembling procedure leads to two distinct layers of P3HT and PCBM, with quite low interpenetration between the two components [28]. The electrodes were thermally evaporated through a shadow mask of 6 mm^2, in a vacuum chamber at 2×10^{-6} mbar. The devices were prepared with three different cathodes prepared by subsequent evaporation steps: LiF (1.5 nm)/Al (100 nm); Ca (20 nm)/Al (100 nm) or Al (100 nm). The current density–voltage (*J–V*) characteristics of the cells were measured at room temperature inside the glove box in nitrogen atmosphere, using a Keithley 2600 sourcemeter under 100 mW/cm^2 solar simulation, with a Class A AM1.5 ABET Sun 2000 solar simulator, as measured with a calibrated KG5 + Si cell. Table 3 collects some relevant experimental device parameters for each device.

Table 3
Overview of experimental device parameters.

Parameter	Symbol	Al	LiF/Al	Ca/Al	Unit
OC voltage	V_{oc}	0.46	0.56	0.63	V
SC current	J_{SC}	6.39	6.67	6.24	mA/cm^2
Fill Factor	*FF*	0.64	0.65	0.71	–

4. Results and discussion

In order to optimize the model parameters, a fitting to the experimental *J–V* data was performed over the range from −0.5 to 1.1 V. Our fitting results are shown in Fig. 2. Table 4 gives the final values of the fit parameters. It should be noted that all these values are consistent with those commonly used in KMC simulations, as we shall see below. The upper part of Table 4 groups the parameters common to all devices. Literature values [38,39] of the cathode work functions have also been included, for comparison purposes. It should be noted that these values refer to the work functions of the "bare" substrate, and do not account for surface contamination effects, often observed in solution processed devices [40].

The relative permittivity was not optimized and was taken as 3.5 for both PCBM and the P3HT. The lattice constant, corresponding to the inter-layer distance, was set to 1 nm. To simulate the solar illumination at an intensity of 100 mW/cm^2, we fixed the exciton generation rate per site at 6×10^{-12} nm^{-3} ps^{-1}. The exciton dissociation rate, w^{exs}, was taken as 20 ps^{-1} [27]. Some test calculations were performed to evaluate the effect of the device size. Increasing the electrode surface area from 0.01 μm^2 to 1 μm^2 was found to change the optimal values of device-specific

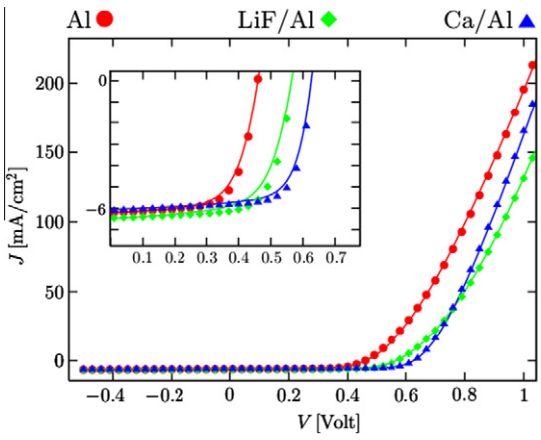

Fig. 2. Experimental (symbols) and simulated (lines) *J–V* curves. The inset shows the region around the V_{OC} in detail.

Table 4
Final values of the model fit parameters for the data shown in Fig. 2. *Experimental values of the cathode work functions were taken from Refs. [38] and [39].

Parameter (symbol)		Value		Unit
Relative perm. (ϵ_r)		3.5		–
Lattice constant (ℓ)		1		nm
Ex. gen. rate (w^{exg})		6×10^{27}		$m^{-3}\,s^{-1}$
Ex. diss. rate (w^{exs})		20		ps^{-1}
Ex. hopping rate (w^{exh})		1.2		ps^{-1}
Ex. decay rate (w^{exd})		8×10^{-4}		ps^{-1}
Gp. decay rate (W^{gpd})		2.3×10^{6}		s^{-1}
PEDOT:PSS/ITO WF (ϕ_{anode})		4.95		eV
P3HT HOMO (E_D^H)		−5.30		eV
	Al	LiF/Al	Ca/Al	
El. mobility (μ_0^{el})	3.0	3.5	2.4	$10^{-3}\,\frac{cm^2}{sV}$
Ho. mobility (μ_0^{ho})	2.0	1.7	4.1	$10^{-4}\,\frac{cm^2}{sV}$
PCBM LUMO (E_A^L)	−4.28	−4.17	−4.11	eV
Cathode WF ($\phi_{cathode}$)	4.28	4.17	4.12	eV
Exp. Cath. WF ($\phi_{cathode}^{exp}$)*	4.28	3.70	2.87	eV

parameters by 5%, with no effect on the main conclusions reported below.

The exciton hopping and decay rates had the highest influence on the absolute magnitude of the current density at negative biases. Our choice ($w^{exh} = 1.2\ ps^{-1}$ and $w^{exd} = 8 \times 10^{-4}\ ps^{-1}$) was dictated by the need to match short-circuit current densities on the order of 6 mA/cm^2. These refer to both donor and acceptor, since the same rate constants were used to model exciton transport in these materials. Using these parameters, the values of the exciton diffusion coefficient ($D_{ex} = 2.0 \times 10^{-3}\ cm^2/s$) and diffusion length ($L_{ex} = 38.72$ nm) were extracted from Eqs. (4) and (6). It is important to note that these estimates are drawn from the continuum distribution of excitons at steady state, and their value does not depend on the exciton hopping length (1 nm). Our value for D_{ex} agrees with that reported by Shaw [41] for P3HT films of varying thickness ($1.8 \times 10^{-3}\ cm^2/s$). Very few experimental studies exist in the literature on exciton transport in PCBM [42,43], which is generally recognized as a weak emitter [44]. The value of $3.33 \times 10^{-5}\ cm^2/s$, calculated starting from the time-resolved emission data published by Cook et al. [42] is two order of magnitude lower than ours. Nonetheless, as noticed by these authors, larger exciton diffusion lengths and coefficients may be expected on the basis of those obtained for C_{60} (up to 40 nm) [45]. Our estimate for L_{ex} looks higher than that of 8–27 nm commonly reported in the literature for P3HT [46], but is substantially lower than the value of 80 nm reported by Ayzner et al. [28] for their P3HT/PCBM bilayers. They attributed this discrepancy to long-range exciton transport mechanisms [30]. The enhanced exciton diffusion length might be a key factor responsible for the power conversion efficiency of our devices (2.5% on the average).

Exciton dissociation leads to the formation of geminate electron–hole pairs. In most DD models, where exciton dynamics is not explicitly taken into account, the rate at which this process occurs is given as an input parameter and kept constant over the entire voltage range. In our model, conversely, its value is given by $\left(N_{L_z}^{ex} + N_{L_z+1}^{ex}\right) W^{exs}$ and may weakly depend on the applied voltage in response to the change in the occupancy numbers (see Eq. (7)). Performing the simulations, we found an average value of $3.18 \times 10^{27}\ m^{-3}\,s^{-1}$ over the full fitting range. This is close to that used in DD simulations [19,47] and indicates that only half of the harvested photons ($6 \times 10^{27}\ m^{-3}\,s^{-1}$) are converted into geminate pairs. A fraction of these pairs do not contribute to photocurrent generation, but recombine at rate W^{gpd}. At short circuit, this fraction was found to be about 23.5% for all devices, finally leading to about 40% internal quantum efficiency (IQE).

Our optimal values for ϕ_{anode} and E_D^H are close to those reported in the literature for these materials [48,49]. A sensitivity test, in which these parameters were varied independently, was carried out to assess their influence on V_{OC} and current density. The results showed that V_{OC} was not affected by ϕ_{anode} but controlled by E_D^H, with a proportionality factor close to one. Both of these findings are consistent with experimental studies carried out on bilayers [50] as well as bulk heterojunctions [48]. The effect of these parameters on the current density is related to the change in the hole injection barrier, $-\phi_{anode} - E_D^H$. Setting its value too high (>0.5 eV) or too low (<0.1 eV) led to a significant decrease in the current density, and the appearance of the so-called "S-curve" [51]. This outcome, presumably associated with charge depletion in the region next to the metal contacts, will be investigated in a forthcoming paper.

To model the effect of using different cathode materials, the remaining parameters in Table 4 were optimized independently for each device. Electron and hole mobilities were slightly adjusted to better approximate experimental current densities at low and high biases, respectively. The fact that no significant mixing of D and A phases has occurred during device assembling [28], enables a comparison with mobility data given in the literature for pure films. Our results are in good agreement with those reported by Waldauf et al. [52] for PCBM $\left(\mu_0^{el} = 3.5 \times 10^{-3}\ cm^2/s/V\right)$, and Choulis et al. [53] for P3HT $\left(\mu_0^{ho} = 3.0 \times 10^{-4}\ cm^2/s/V\right)$. This confirms the soundness of our model and justifies the assumption of pure phases in device representation.

As can be seen from Table 3, changing the top electrode material has little influence on the V_{OC}, despite the considerable differences in the cathode work functions (bottom line of Table 4). A total variation of only 0.17 V was observed on going from Al ($\phi_{cathode}^{exp} = 4.28$ eV) to Ca ($\phi_{cathode}^{exp} = 2.87$ eV). This behavior, similar to that observed in bulk heterojunctions (BHJs) [38,54], suggests that these metals may form ohmic contacts with PCBM by a mechanism known as Fermi level pinning [54–56]. When this occurs, the work function of the metal aligns to that of the semiconductor via charge transfer across the metal/organic interface. The same phenomenon is sometimes discussed in terms of the formation of an interface dipole [57,58]. It is certainly a very general mechanism but, when it comes to discussing specific situations, the analysis and theoretical

interpretation of the experimental data can be somewhat controversial and a subject of debate.

Our optimized values for E_A^L and $\phi_{cathode}$, given in Table 4, support the existence of ohmic contacts at the Cathode/PCBM interface. In each case, the best fits were obtained by pinning the cathode work function at the PCBM LUMO energy level. Owing to the accumulation of electrons close to the cathode, this level does not represent the effective transport level of electrons injected in the acceptor. Taking into account the effect of both the image charge and the electrostatic potential, we found this level to be located at about −3.9 eV, which roughly agrees with the PCBM LUMO energy commonly reported in the literature (−3.7 eV [59]).

The small differences in E_A^L values are somewhat unexpected and are likely associated with our approximate description of the metal/semiconductor interface. The development of a better model of the interfacial dipole layer is currently in progress. This should allow us to use a single E_A^L value for all devices.

The influence of E_A^L and $\phi_{cathode}$ on the V_{OC} is entirely similar to that above observed for E_D^H and ϕ_{anode}. Again, the position of the V_{OC} is essentially controlled by energy levels of the semiconductors (E_A^L and E_D^H), rather than by the metal work functions. This outcome has quite a simple explanation. Changing $\phi_{cathode}$ (ϕ_{anode}) alters both the built-in voltage and the electron (hole) injection barrier height. The effects of these changes nearly cancel each other, leaving the V_{OC} unaffected. On the other hand, changing $E_A^L\left(E_D^H\right)$, only affects the electron (hole) injection barrier height and, consequently, the V_{OC} position. This provides a qualitative explanation to the negligible dependence of V_{OC} on the electrode work function, which has been experimentally observed in a number of OSCs [50], including bulk heterojunctions [38].

5. Conclusions

KMC is a powerful tool to investigate the J–V properties of OSCs. Its applicability to the study of devices characterized by ohmic behavior is nonetheless limited by the small-barrier problem. To overcome it, we have developed a one-dimensional coarse-grained (1DCG) numerical approach to photocurrent generation in bilayer heterojunction solar cells. The 1DCG model of the device has been derived from the three-dimensional one used in KMC simulations and it incorporates the generation, transport and recombinations of charge carriers, excitons, and electron/hole pairs. The model has been used to investigate the J–V properties of three Cathode/PCBM/P3HT/PEDOT:PSS/ITO bilayers with high fill factors. From the fitting to the experimental data, we conclude the short-circuit current density to be mainly associated with the high exciton diffusion length, which arises from the deposition of the PCBM overlayer. The fact that electron and hole mobilities agree with the data given in the literature for pure films is consistent with the assumption of pure phases separated by a sharp and flat interface. The weak dependence of V_{OC} on the cathode work functions points to the existence of ohmic contacts at the Cathode/PCBM interface. Our fitting results confirms this expectation, which is also consistent with the mechanism of Fermi level pinning, already observed in BHJs. A qualitative explanation of this outcome has been provided, which involves a trade off between the built-in voltage and the electron injection barrier height. Additionally, we have shown that, in our model, the V_{OC} is controlled by the energy levels of the acceptor and the donor.

It is worth discussing the analogies and differences between our model and existing ones. These essentially include KMC and DD models, since, to our knowledge, master equation approaches have not yet been applied to full OSC modeling. Our method strongly relies on the KMC framework, where all microscopic phemomena can be described by means of simple equations. This considerably simplifies the implementation of effects that require more complex expressions in DD approaches. An example is given by the mathematical expressions that govern charge injection. In the model proposed by Barker et al. [19], charge injection is described by a complex equation derived from the Scott–Malliaras model [9]. In our model, conversely, this is simply treated as a hopping process across the metal–organic interface.

The main advantage of our model, compared to KMC, lies in the possibility to model OSC devices characterized by ohmic behavior. Use of coarse graining in both space and time significantly reduces the computational cost. The calculation of a full J–V curve takes about 25–30 min on a single processor. At the same time, coarse-graining suffers of some limitations. Spatially averaging the electrostatic interactions over the coarse cell can be expected to underestimate the influence of correlation effects. These play an important role in particle transport and electron–hole recombination. Furthermore, as pointed out by Houili et al. [26], continuum, mean-field approaches fail to treat the Coulomb interaction correctly at both short and long distances. This aspect has recently been investigated in detail by van der Holst and co-workers [60], who have shown that one-dimensional DD models tend to overestimate the KMC current density in single-type carrier devices characterized by small injection barriers (<0.3 eV). Owing to the small-barrier problem, the comparison between 1DCG and KMC approaches has not been attempted in the current work. We shall address such a comparison in a forthcoming paper, for systems computationally tractable by both methods.

In contrast to KMC, drift–diffusion has more extensively been compared with experimental J–V data. Our method shares with DD approaches the use of geminate pairs to describe carrier generation and recombination at the interface. Apart from this analogy, which has been discussed above, considerable differences exist in the way the processes underlying photocurrent generation are simulated. It is therefore surprising that, as far as the dependence of the V_{OC} on the cathode work function is considered, our model behaves similarly to that developed by Barker et al. [19] and Cheyns et al. [21].

We have neglected both energy and disorder within the photoactive layer [1,10,35,61–63]. The former plays a role in the definition of the average transport levels, and can be expected to influence the hopping rates at all regimes. Its inclusion is necessary to account for the temperature dependence of the carrier mobilities. The assumption of

equally spaced hopping sites clearly conflicts with the concept of transport in disordered solids. Positional disorder is also necessary for the description of more complex morphologies, such as bulk heterojunctions and partially intermixed bilayers. Modelling both effects would be difficult and perhaps also questionable within the present approach. Instead, their introduction in standard, three-dimensional KMC algorithms is almost straightforward. We are currently working in order to improve the speed and accuracy of such simulations, along the lines of our earlier work on electrostatic interactions [27].

Acknowledgments

This work was financially supported by ENI and by Fondazione Cariplo, Grant No. 2011–0349 (PLENOS).

Appendix A. Calculation of the electrostatic interactions

The term $\Delta\overline{E}^{C}_{i,j}$ in Eq. (15) accounts for the change in the total electrostatic energy associated with the hopping of one charge from the i-th to the j-th layer. We write it as the sum of two contributions:

$$\Delta\overline{E}^{C}_{i,j} = \Delta\overline{E}^{S}_{i,j} + \Delta\overline{E}^{T}_{i,j}, \tag{A.1}$$

where $\Delta\overline{E}^{S}_{i,j}$ is the self-interaction between the hopping charge and its images inside the electrodes, and $\Delta\overline{E}^{T}_{i,j}$ is the cross-interaction term. The first term can be written as:

$$\Delta\overline{E}^{S}_{i,j} = \overline{E}^{S}_{j} - \overline{E}^{S}_{i} = -\frac{1}{2}U(\mathbf{v}_j) + \frac{1}{2}U(\mathbf{v}_i), \tag{A.2}$$

where $\mathbf{v}_{i(j)}$ is distance between the charge and its closest image before (after) hopping, while U the electrostatic potential energy function. Note that, for a charge occupying the i-th layer, the closest image can be located at $i' = -i$ (across the cathode) or $i' = 2M_z + 2 - i$ (across the anode). In Ref. [27] we have shown that, in a device with semi-infinite metallic electrodes, the distribution of the charges is periodic in three dimensions and U can be evaluated exactly using the Ewald summation method. Here, for simplicity, we calculate U using a cutoff formula [27], setting the cutoff distance to twice the active layer thickness ($r_{cut} = 2(M_z + 1)\ell$). To model charge injection and extraction, Eq. (A.2) is modified by setting $\overline{E}^{S}_{0} = \overline{E}^{S}_{M_z+1} = 0$.

The second term in Eq. (A.1) accounts for the interactions between the hopping particle and all other charges, excluding the closest image. The starting point for its construction is the average pairwise interaction energy between two charges located at the i-th and j-th layer, $\overline{U}_{i,j}$. This is:

$$\overline{U}_{i,j} = \frac{\sum_{k\in\Omega_i}\sum'_{l\in\Omega_j} U(\mathbf{r}_{kl}) e^{-U(\mathbf{r}_{kl})/k_BT}}{\sum_{k\in\Omega_i}\sum'_{l\in\Omega_j} e^{-U(\mathbf{r}_{kl})/k_BT}} \approx \frac{1}{M^2_{xy}}\sum_{k\in\Omega_i}\sum_{l\in\Omega_j} U(\mathbf{r}_{kl}), \tag{A.3}$$

where the prime excludes from the summation the terms with $k = l$, when $i = j$. $\Omega_{i(j)}$ refers to the set of possible sites for a particle in the $i(j)$-th layer, while $\mathbf{r}_{kl}$ represents the distance between the sites k and l. In our bilayer model, the case $i = j$ occurs for equally charged carriers, but not for oppositely charged ones where $|i - j| \geqslant 1$. The approximation of Eq. (A.3) is appropriate at large interlayer distances (we used it above 7 nm). At shorter distances, $\overline{U}_{i,j}$ was evaluated numerically by two sets of fine-grid KMC simulations, with two charges constrained to move on two layers facing each other along the z axis. The resulting potential functions will be denoted by $\overline{U}_{i,j^-}$ (for oppositely charged carriers) and $\overline{U}_{i,j^+}$ (for equally charged carriers). The results of these calculations are reported in Fig. A.1 for $\ell = 1$ nm and $M_x = M_y = 100$.

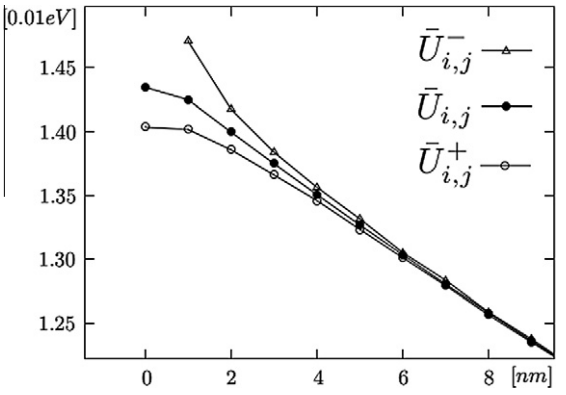

Fig. A.1. Average pairwise energies as a function of the separation distance for $\ell = 1$ nm. Electron and holes mobilities were both taken as 10^{-7} m^2/V/s. KMC averages were estimated with an accuracy of 5×10^{-5} eV (smaller than symbol size).

Next, we focus on the pairwise interactions that contribute to $\Delta\overline{E}^{T}_{i,j}$, i.e. those subject to change during the hopping process. A schematic view of such interactions is given in Fig. A.2, along with the initial (*ini*) and final (*end*) states that characterize charge hopping at the coarse-grained level. Hereafter, we shall assign to these states single-particle "interaction" energies, namely $\overline{E}^{T,ini}_{i}$ and $\overline{E}^{T,end}_{j}$, so that $\Delta\overline{E}^{T}_{i,j}$ can be written as $\overline{E}^{T,end}_{j} - \overline{E}^{T,ini}_{i}$. $\overline{E}^{T,ini}_{i}$ quantifies the energy loss associated with the "removal" of a charge from the i-th layer. It can be written as the sum of intra- and inter-layer contributions [32]. The inter-layer contribution, $\overline{E}^{T,ini}_{i,inter}$, accounts for the interactions

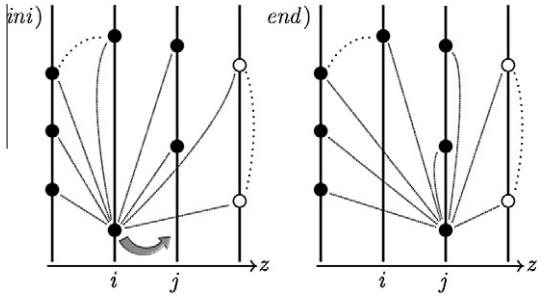

Fig. A.2. A simplified, two-dimensional sketch of the pairwise interactions that contribute to $\Delta\overline{E}^{T}_{i,j}$ (stipples), along with the initial (*ini*) and final (*end*) states that characterize electron hopping. Dotted lines identify interactions that do not change during the hopping process, and, therefore, do not contribute to $\Delta\overline{E}^{T}_{i,j}$. Particle positions along the vertical axis are arbitrary.

between the hopping particle in the i-th layer and those in the other layers, as well as their images:

$$\overline{E}^{T,ini}_{i,inter} = \begin{cases} +\sum\limits_{\substack{k=1\\k\neq i}}^{L_z} N^{el}_k \overline{V}^{+}_{i,k} \; - \sum\limits_{k=L_z+1}^{M_z} N^{ho}_k \overline{V}^{-}_{i,k} & 1 \leqslant i \leqslant L_z \\ -\sum\limits_{k=1}^{L_z} N^{el}_k \overline{V}^{-}_{i,k} \; + \sum\limits_{\substack{k=L_z+1\\k\neq i}}^{M_z} N^{ho}_k \overline{V}^{+}_{i,k} & L_z+1 \leqslant i \leqslant M_z, \end{cases} \tag{A.4}$$

where $\overline{V}^{\pm}_{i,k} = \overline{U}^{\pm}_{i,k} - \overline{U}^{\pm}_{i,k'}$. k' defines the position of the closest image for a particle in the k-th layer, and can either be $-k$ or $2M_z + 2 - k$, as mentioned above. The construction of the terms $\overline{V}^{\pm}_{i,k}$ is illustrated in Fig. A.3. Eq. (A.4) can be used in 1DCG or CG-KMC simulations, indifferently.

The second contribution to $\overline{E}^{T,ini}_i$, $\overline{E}^{T,ini}_{i,intra}$, represents the energy of a particle interacting with others within the same layer. Its expression differs from that one would obtain in CG-KMC $\left(N^{el(ho)}_i - 1\right)\overline{V}^{+}_{i,i}$, for electrons (holes). The reason is that, in CG-KMC, the occupancy numbers vary discretely at each iteration, while, in our model, they change continuously. To account for this difference, we replace $\left(N^{el(ho)}_i - 1\right)$ with its time average $\left\langle N^{el(ho)}_i - 1\right\rangle$, in the above expression. In the following, we shall rewrite this average in a form suitable for 1DCG simulations, e.g. as a function of $N^{el(ho)}_i$. For simplicity, we consider the case of electrons, writing N^{el}_i as a time average:

$$N^{el}_i = \langle N^{el}_i \rangle = \frac{1}{\tau}\sum_m N^{el}_{i(m)}\tau_m = \sum_{n=1}^{M_{xy}} n f_i(n), \tag{A.5}$$

where $N^{el}_{i(m)}$ is the number of electrons at the each step in an hypothetical KMC simulation, while τ the total simulation time. The function $f_i(n)$ represents the fraction of time the i-th layer is occupied by n electrons:

$$f_i(n) = \frac{1}{\tau}\sum_m \tau_m \quad \forall m : n = N^{el}_{i(m)}. \tag{A.6}$$

According to Eq. (A.6), one has:

$$\sum_{n=0}^{M_{xy}} f_i(n) = 1. \tag{A.7}$$

From (A.5) it follows that:

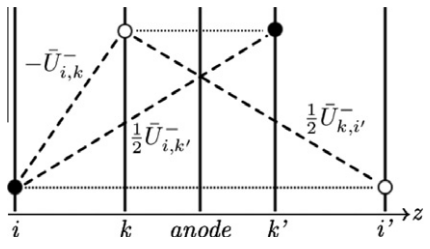

Fig. A.3. Construction of the term $\overline{V}^{-}_{i,k}$ when $k' = 2M_z + 2 - k$. Electrons are represented by filled circles, holes by open ones. Dashed lines represent the interactions that contribute to $\overline{V}^{-}_{i,k}$. Dotted lines connect the charges with their self-images across the anode. Note that $\overline{U}^{-}_{k,i'} \equiv \overline{U}^{-}_{i,k'}$, by symmetry. $\overline{V}^{+}_{i,k}$ can be obtained in the same way.

$$\left\langle N^{el}_i - 1\right\rangle = \sum_{n=1}^{M_{xy}} (n-1) f_i(n). \tag{A.8}$$

Combining Eqs. (A.7) and (A.8) leads to:

$$\left\langle N^{el}_i - 1\right\rangle = \left\langle N^{el}_i\right\rangle - 1 + f_i(0). \tag{A.9}$$

Similarly, one has:

$$\left\langle N^{el}_i + 1\right\rangle = \left\langle N^{el}_i\right\rangle + 1 - f_i(0). \tag{A.10}$$

Similar formulas hold for holes. Given Eq. (A.9) and the corresponding expression for holes, the intra-layer energy takes the following form:

$$\overline{E}^{T,ini}_{i,intra} = \begin{cases} \left(N^{el}_i - 1 + f_i(0)\right)\overline{V}^{+}_{i,i} & 1 \leqslant i \leqslant L_z \\ \left(N^{ho}_i - 1 + f_i(0)\right)\overline{V}^{+}_{i,i} & L_z + 1 \leqslant i \leqslant M_z. \end{cases} \tag{A.11}$$

The only unknown in Eq. (A.11) is the value of $f_i(0)$ at all layers. This corresponds to the fraction of time the i-th layer is not occupied by electrons, or holes. To find it out, we make the following hypothesis:

$$f_i(n) = (n+1)\, C_i f_i(n+1), \quad \text{for} \quad 0 \leqslant n \leqslant M_{xy} - 1, \tag{A.12}$$

where C_i is constant at each layer. Hereafter, we shall demonstrate that $f_i(0)$ can be approximated as:

$$f_i(0) \simeq \left(\sum_{n=0}^{M_{xy}} \frac{1}{n! C_i^n}\right)^{-1}, \tag{A.13}$$

when $C_i = 1/N^{el(ho)}_i$. For simplicity, we consider again the case of electrons. First, we rewrite N^{el}_i combining Eqs. (A.5) and (A.12):

$$N^{el}_i = f_i(0)\sum_{n=1}^{M_{xy}} \frac{1}{(n-1)!\, C_i^n}. \tag{A.14}$$

Using Eqs. (A.12) and (A.7) can be written as:

$$1 = f_i(0)\sum_{n=0}^{M_{xy}} \frac{1}{n! C_i^n}. \tag{A.15}$$

For M_{xy} large, we may assume $M_{xy} - 1 \approx M_{xy}$, thereby writing Eq. (A.15) as:

$$1 = f_i(0)\sum_{n=1}^{M_{xy}} \frac{C_i}{(n-1)! C_i^n}. \tag{A.16}$$

Both Eqs. (A.14) and (A.16) must hold true for $1 \leqslant i \leqslant L_z$. This can only be accomplished setting $C_i = 1/N^{el}_i$ in this interval, and $C_i = 1/N^{ho}_i$ for $L_z + 1 \leqslant i \leqslant M_z$. The calculation of $f_i(0)$ via Eq. (A.13), can be performed truncating the sum at $n \simeq 50$, without significant loss in accuracy.

In analogy with $\overline{E}^{T,ini}_i$, the final energy, $\overline{E}^{T,end}_j$, can be interpreted as the gain in energy associated with the "creation" of a charge in the j-th layer. To save CPU time, this energy can be evaluated with respect to the initial state, as:

$$\overline{E}^{T,end}_j = \overline{E}^{T,ini}_j + (1 - f_j(0))\overline{V}^{+}_{j,j} - (1 - f_i(0))\overline{V}^{+}_{j,i}. \tag{A.17}$$

During the hopping process, the occupancy numbers of the i-th and j-th layers change to $\left\langle N^{el(ho)}_i - 1\right\rangle$ and $\left\langle N^{el(ho)}_j + 1\right\rangle$,

respectively. The latter two terms in Eq. (A.17) account for this change thorugh Eqs. (A.9) and (A.10).

For charge injection and extraction the situation is slightly different. Charge injection leads to the generation of one electron (hole) in the first layer next to the cathode (anode). To cast $\Delta\overline{E}^{T}_{i,j}$ we consider the pairwise interactions that are formed during this process. This leads to:

$$\Delta\overline{E}^{T}_{i,j} = \overline{E}^{T,ini}_{j} + (1 - f_j(0))\,\overline{V}^{+}_{j,j}, \tag{A.18}$$

where $i = 0(M_z + 1)$ and $j = 1(M_z)$ for electrons (holes). Finally, during charge extraction, the charge is removed from the device, therefore:

$$\Delta\overline{E}^{T}_{i,j} = -\overline{E}^{T,ini}_{i}, \tag{A.19}$$

where $i = 1(M_z)$ and $j = 0(M_z + 1)$.

References

[1] J.-L. Bredas, J.E. Norton, J. Cornil, V. Coropceanu, Acc. Chem. Res. 42 (2009) 1691–1699;
J. Peet, A.J. Heeger, G.C. Bazan, Acc. Chem. Res. 42 (2009) 1700–1708;
P. Heremans, D. Cheyns, B.P. Rand, Acc. Chem. Res. 42 (2009) 1740–1747;
J. Roncali, Acc. Chem. Res. 42 (2009) 1719–1730;
J. Nelson, J.J. Kwiatkowski, J. Kirkpatrick, J.M. Frost, Acc. Chem. Res. 42 (2009) 1768–1778;
W.J. Potscavage Jr., A. Sharma, B. Kippelen, Acc. Chem. Res. 42 (2009) 1758–1767.

[2] R.F. Service, Science 332 (2011) 293;
Y. Liang, L. Yu, Acc. Chem. Res. 43 (2010) 1227–1236;
S.H. Park, A. Roy, S. Beaupré, S. Cho, N. Coates, J.S. Moon, M. Leclerc, K. Lee, D. Moses, A.J. Heeger, Nature Photonics 3 (2009) 297–302;
T.-Y. Chu, J. Lu, S. Beaupré, Y. Zhang, J.-R. Pouliot, S. Wakim, J. Zhou, M. Leclerc, Z. Li, J. Ding, Y. Tao, JACS 133 (2011) 4250–4253;
Y. Liang, Z. Xu, J. Xia, S.-T. Tsai, Y. Wu, G. Li, C. Ray, L. Yu, Adv. Mater. 22 (2010) E135–E138.

[3] W.-Y. Wong, C.-L. Ho, Acc. Chem. Res. 43 (2010) 1246–1256;
D. Yu, K. Park, M. Durstock, L. Dai, J. Phys. Chem. Lett. 2 (2011) 1113–1118;
P.A. Troshin, H. Hoppe, A.S. Peregudov, M. Egginger, S. Shokhovets, G. Gobsch, N.S. Sariciftci, V.F. Razumov, ChemSusChem 4 (2011) 119–124.

[4] M.-G. Kang, T. Xu, H.J. Park, X. Luo, L.J. Guo, Adv. Mater. 22 (2010) 4378–4383;
G. Dennler, M.C. Scharber, T. Ameri, P. Denk, K. Forberich, C. Waldauf, C.J. Brabec, Adv. Mater. 20 (2008) 579–583.

[5] J.-S. Kim, W.-S. Chung, K. Kim, D.Y. Kim, K.-J. Paeng, S.M. Jo, S.-Y. Jang, Adv. Funct. Mater. 20 (2010) 3538–3546;
P. Kovacik, G. Sforazzini, A.G. Cook, S.M. Willis, P.S. Grant, H.E. Assender, A.A.R. Watt, Appl. Mater. Interfaces 3 (2011) 11–15;
J. Peet, M.L. Senatore, A.J. Heeger, G.C. Bazan, Adv. Mater. 21 (2009) 1521–1527.

[6] S. Selberherr, Analysis and Simulation of Semiconductor Devices, Springer-Verlag, Wien, Germany, 1984.

[7] A.F. Voter, Introduction to the Kinetic Monte Carlo method, in: K.E. Sickafus, E.A. Kotomin, B.P. Uberuaga (Eds.), Radiation Effects in Solids, Springer, NATO Publishing Unit, Dordrecht, Netherlands, 2006, pp. 1–23.

[8] G.G. Malliaras, J.C. Scott, J. Appl. Phys. 85 (1999) 7426–7432;
P.W.M. Blom, M.J.M. de Jong, S. Breedijk, Appl. Phys. Lett. 71 (1997) 930–933;
D.J. Pinner, R.H. Friend, N. Tessler, J. Appl. Phys. 86 (1999) 5116–5130.

[9] J.C. Scott, G.G. Malliaras, Chem. Phys. Lett. 299 (1999) 115–119.

[10] H. Bässler, Phys. Status Solidi B 175 (1993) 15–56;
V.I. Arkhipov, U. Wolf, H. Bässler, Phys. Rev. B 59 (1999) 7514–7520;
U. Wolf, V.I. Arkhipov, H. Bässler, Phys. Rev. B 59 (1999) 7507–7513.

[11] R.A. Marsh, C. Groves, N.C. Greenham, J. Appl. Phys. 101 (2007) 083509;
L.Y. Meng, Y. Shang, Q.K. Li, Y.F. Li, X.W. Zhan, Z.G. Shuai, R.G.E. Kimber, A.B. Walker, J. Phys. Chem. B 114 (2010) 36–41.

[12] A. Miller, E. Abrahams, Phys. Rev. 120 (1960) 745–755.

[13] The overall probability of extraction events increases during the simulation until the steady state is reached. At this point, the rates of charge injection and extraction become each other equal.

[14] A.F. Voter, Introduction to the time-scale problem, in: M. Laudon, B. Romanowicz (Eds.), Proceedings of Computational Nanoscience and Nanotechnology, Computational Publications, Cambridge, MA, 2002, pp. 128–131.

[15] A. Chatterjee, A.F. Voter, J. Chem. Phys. 132 (2010) 194101.

[16] P.K. Watkins, A.B. Walker, G.L.B. Verschoor, Nano Lett. 5 (2005) 1814–1818.

[17] F. Yang, F.R. Forrest, ACS Nano 2 (2008) 1022–1032.

[18] R.G.E. Kimber, A.B. Walker, G.E. Schröder-Turk, D.J. Cleaver, Phys. Chem. Chem. Phys. 12 (2010) 844–851.

[19] J.A. Barker, C.M. Ramsdale, N.C. Greenham, Phys. Rev. B 67 (2003) 075205.

[20] R. Häusermann, E. Knapp, M. Moos, N.A. Reinke, T. Flatz, B. Ruhstaller, J. Appl. Phys. 106 (2009) 104507;
K. Maturová, S.S. van Bavel, M.M. Wienk, R.A.J. Janssen, M. Kemerink, Adv. Funct. Mater. 21 (2011) 261;
T. Kirchartz, B.E. Pieters, K. Taretto, U. Rau, J. Appl. Phys. 104 (2008) 094513;
L.J.A. Koster, V.D. Mihailetchi, R. Ramaker, P.W.M. Blom, App. Phys. Lett. 86 (2005).

[21] D. Cheyns, J. Poortmans, P. Heremans, C. Deibel, S. Verlaak, B.P. Rand, J. Genoe, Phys. Rev. B 77 (2008) 165332.

[22] J.A. Freire, G. Voss, J. Chem. Phys. 122 (2005) 124705.

[23] N. Rappaport, Y. Preezant, N. Tessler, Phys. Rev. B 76 (2007) 235323.

[24] J.J.M. van der Holst, M.A. Uijttewaal, B. Ramachandhran, R. Coehoorn, P.A. Bobbert, G.A. de Wijs, R.A. de Groot, Phys. Rev. B 79 (2009) 085203.

[25] W.F. Pasveer, J. Cottaar, C. Tanase, R. Coehoorn, P.A. Bobbert, P.W.M. Blom, D.M. de Leeuw, M.A.J. Michels, Phys. Rev. Lett. 94 (2005) 206601.

[26] H. Houili, E. Tutiš, I. Batistić, L. Zuppiroli, J. Appl. Phys. 100 (2006) 033702.

[27] M. Casalegno, G. Raos, R. Po, J. Chem. Phys. 132 (2010) 094705.

[28] A.L. Ayzner, C.J. Tassone, S.H. Tolbert, B.J. Schwartz, J. Phys. Chem. C 113 (2009) 20050.

[29] V.S. Gevaerts, L.J.A. Koster, M.M. Wienk, R.A.J. Janssen, Appl. Mater. Interfaces 3 (2011) 3252–3255.

[30] H. Najafov, B. Lee, Q. Zhou, L.C. Feldman, V. Podzorov, Nature Mater. 9 (2010) 938–943;
D.C. Coffey, A.J. Ferguson, N. Kopidakis, G. Rumbles, ACS Nano 4 (2010) 5437–5445.

[31] M.A. Katsoulakis, D.G. Vlachos, J. Chem. Phys. 119 (2003) 9412;
A. Chatterjee, D.G. Vlachos, J. Chem. Phys. 121 (2004) 11420.

[32] J.G. Dai, W.D. Seider, T.J. Sinno, Chem. Phys. 128 (2008) 194705.

[33] Günes, H. Neugebauer, N.S. Sariciftci, Chem. Rev. Washington, DC 107 (2007) 1324.;
H. Hoppe, N.S. Sariciftci, J. Mater. Res. 19 (2004) 1924–1945;
R. Po, M. Maggini, N. Camaioni, J. Phys. Chem. C 114 (2010) 695–706;
B.C. Thompson, J.M.J. Frèchet, Angew. Chem. 47 (2008) 58–77.

[34] A. Einstein, Ann. Phys. 17 (1905) 549–560;
M.V. Smoluchowski, Ann. Phys. 21 (1906) 756–780.

[35] C. Groves, R.A. Marsh, N.C. Greenham, J. Chem. Phys. 129 (2008) 114903.

[36] P. Langevin, Ann. Chim. Phys. 7 (1903) 433–530.

[37] A. Maurano, C.G. Shuttle, R. Hamilton, A.M. Ballantyne, J. Nelson, W. Zhang, M. Heeney, J.R. Durrant, J. Phys. Chem. C 115 (2011) 5947–5957;
A. Pivrikas, N.S. Sariciftci, G. Juska, R. Österbacka, Progress in Photovoltaics: Research and Applications 15 (2007) 677;
C.G. Shuttle, B. O'Regan, A.M. Ballantyne, J. Nelson, D.D.C. Bradley, J.R. Durrant, Phys. Rev. B 78 (2008) 4.

[38] C.J. Brabec, N.S. Sariciftci, J.C. Hummelen, Adv. Funct. Mater. 11 (2001) 374–380.

[39] V.D. Mihailetchi, P.W.M. Blom, J.C. Hummelen, M.T. Rispens, J. Appl. Phys. 94 (2003) 6849.

[40] J. Hwang, A. Wan, A. Kahn, Mater. Sci. Eng. R 64 (2009) 1–31;
I. Lange, J.C. Blakesley, J. Frisch, A. Vollmer, N. Koch, D. Neher, Phys. Rev. Lett. 106 (2011) 216402.

[41] P.E. Shaw, A. Ruseckas, I.D.W. Samuel, Adv. Mater. 20 (2008) 3516.

[42] S. Cook, A. Furube, R. Katoh, L. Han, Chem. Phys. Lett. 478 (2009) 33–36.

[43] S. Cook, R. Katoh, A. Furube, J. Phys. Chem. C 113 (2009) 2547–2552.

[44] G.F. Burkhard, E.T. Hoke, S.R. Scully, M.D. McGehee, Nano Lett. 9 (2009) 4037–4041.

[45] P. Peumans, A. Yakimov, S.R. Forrest, J. Appl. Phys. 93 (2003) 3693–3723.

[46] P. Shaw, A. Ruseckas, I. Samuel, Adv. Mater. 20 (2008) 3516–3520;
A. Huijser, T.J. Savenije, A. Shalav, L.D. Siebelles, J. Appl. Phys. 104 (2008) 034505;
S. Cook, H. Liyuan, A. Furube, R. Katoh, J. Phys. Chem. C 114 (2010) 10962–10968.
[47] L.J.A. Koster, E.C.P. Smits, V.D. Mihailetchi, P.W.M. Blom, Phys. Rev. B 72 (2005) 085205.
[48] M.C. Scharber, D. Mühlbacher, M. Koppe, P. Denk, C. Waldauf, A.J. Heeger, C.J. Brabec, Adv. Mater. 18 (2006) 789–794.
[49] K. Kim, J.W. Shin, Y.B. Lee, M.Y. Cho, S.H. Lee, D.H. Park, D.K. Jang, C.J. Lee, J. Joo, ACS Nano 4 (2010) 4197–4205;
M. Onoda, K. Tada, A.A. Zakhidov, K. Yoshino, Thin Solid Films 331 (1998) 76–81.
[50] W.J. Potscavage, A. Sharma Jr., B. Kippelen, Acc. Chem. Res. 42 (2009) 1758–1767.
[51] B.T. de Villers, C.J. Tassone, S.H. Tolbert, B.J. Schwartz, J. Phys. Chem. C 113 (2009) 18978–18982.
[52] C. Waldauf, P. Schilinsky, M. Perisutti, J. Hauch, C.J. Brabec, Adv. Mater. 15 (2003) 2084–2088.
[53] S.A. Choulis, Y. Kim, J. Nelson, D.D.C. Bradley, M. Giles, M. Shkunov, I. McCulloch, Appl. Phys. Lett. 85 (2004) 3890–3892.
[54] R. Steim, F.R. Koglera, C.J. Brabec, J. Mater. Chem. 20 (2010) 2499–2512.
[55] L.J. Brillson, Surf. Sci. Rep. 2 (1982) 123–326;
H. Ishii, K. Sugiyama, E. Ito, K. Seki, Adv. Mater. 11 (1999) 605–625;
R.T. Tung, Phys. Rev. B 64 (2001) 205310.
[56] S. Braun, W.R. Salaneck, M. Fahlman, Adv. Mater. 21 (2009) 1450–1472.
[57] O.L.A. Monti, M.P. Steele, Phys. Chem. Chem. Phys. 12 (2010) 12390–12400.
[58] A. Natan, L. Kronik, H. Haick, R.T. Tung, Adv. Mater. 19 (2007) 4103–4117.
[59] Y. Shirota, H. Kageyama, Chem. Rev. 107 (2007) 953–1010.
[60] J.J.M. van der Holst, F.W.A. van Oost, R. Coehoorn, P.A. Bobbert, Phys. Rev. 83 (2011) 085206.
[61] C.R. McNeill, N.C. Greenham, Adv. Mater. 21 (2009) 3840–3850;
B.A. Gregg, J. Phys. Chem. Lett. 2 (2011) 3013–3015.
[62] S.V. Novikov, D.H. Dunlap, V.M. Kenkre, P.E. Parris, A.V. Vannikov, Phys. Rev. Lett. 81 (1998) 4472–4475.
[63] C. Deibel, T. Strobel, V. Dyakonov, Phys. Rev. Lett. 103 (2009) 036402;
J.M. Frost, F. Cheynis, S.M. Tuladhar, J. Nelson, Nano Lett. 6 (2006) 1674–1681.